



FACULTAD DE CIENCIAS  
UNIVERSIDAD DE CANTABRIA

---

**Search for dark matter production in  
association with top quarks in the  
dilepton final state at  $\sqrt{s} = 13$  TeV**

---

A thesis submitted in fulfillment of the requirements for the  
**Degree of Doctor of Philosophy**

---

Written by  
**Cédric Prieëls**

Under the supervision of  
**Jónatan Piedra Gómez**  
**Pablo Martínez Ruiz del Árbol**

Santander, June 2020



# **Abstract**



# **Resumen**



## Acknowledgments



# Acronyms used

<b>SM</b>	Standard Model	<b>NFW</b>	Navarro-Frenk-White
<b>DM</b>	Dark Matter	<b>LAT</b>	Fermi Large Telescope
<b>LHC</b>	Large Hadron Collider	<b>IACT</b>	Imaging Atmospheric Cherenkov Telescopes
<b>CMS</b>	Compact Muon Solenoid	<b>CTA</b>	Cherenkov Telescope Array
<b>ATLAS</b>	A Toroidal LHC ApparatuS	<b>AMS</b>	Alpha Magnetic Spectrometer
<b>CERN</b>	European Council for Nuclear Research	<b>EFT</b>	Effective Field Theory
<b>QFT</b>	Quantum Field Theory	<b>ISR</b>	Initial State Radiation
<b>CMB</b>	Cosmic Microwave Background	<b>DMWG</b>	Dark Matter Working Group
<b>ML</b>	Machine Learning	<b>MET</b>	Missing Transverse Energy
<b>MFV</b>	Minimal Flavour Violation	<b>VBF</b>	Vector Boson Fusion
<b>WIMP</b>	Weakly Interactive Massive Particle	<b>BR</b>	Branching Ratio
<b>PF</b>	Particle Flow	<b>LEP</b>	Large Electron Positron collider
<b>BSM</b>	Beyond the Standard Model	<b>ALICE</b>	A Large Ion Collider Experiment
<b>MACHO</b>	Massive Compact Halo Object	<b>PS</b>	Proton Synchrotron
<b>MSSM</b>	Minimal Supersymmetric Standard Model	<b>SPS</b>	Super Proton Synchrotron
<b>SI</b>	Spin Independent	<b>PU</b>	Pile Up
<b>SD</b>	Spin Dependent	<b>PV</b>	Primary Vertex
<b>CL</b>	Confidence Level	<b>ECAL</b>	Electromagnetic Calorimeter
<b>QCD</b>	Quantum ChromoDynamics	<b>HCAL</b>	Hadronic Calorimeter
<b>ADMX</b>	Axion Dark Matter Experiment	<b>DT</b>	Drift tube
<b>CAST</b>	CERN Axion Solar Telescope	<b>CSC</b>	Cathode Strip Chamber
<b>IAXO</b>	International Axion Observatory	<b>RPC</b>	Resistive Plate Chamber
<b>LNGS</b>	Laboratori Nazionali del Gran Sasso	<b>TIB/TBD</b>	Tracker Inner Barrel and Disks
<b>UED</b>	Universal Extra Dimensions	<b>TOB</b>	Tracker Outer Barrel

**TEC** Tracker EndCap

**GSF** Gaussian Sum Filter

**HO** Hadron Outer

**MVA** Multi-Variate Analysis

**LS** Long Shutdown

**CSV** Combined Secondary Vertex

**GEM** Gas Electron Multiplier

**DNN** Deep Neural Network

**L1** Level-1 Trigger

**PUPPI** Pileup Per Particle Identification

**HLT** High-Level Trigger

**BW** Breit-Wigner

**DAQ** Data Acquisition System

**MC** Monte Carlo

**DQM** Data Quality Monitoring

**UE** Underlying Event

**DCS** Detector Control System

**PDF** Parton Density Function

**WP** Working Point

**LO** Leading Order

**SC** Super Cluster

**NLO** Next to Leading Order

# Contents

<b>1</b>	<b>The experimental setup</b>	<b>1</b>
1.1	The Large Hadron Collider (LHC) accelerator . . . . .	1
1.1.1	The LHC in a nutshell . . . . .	2
1.1.2	LHC key parameters . . . . .	3
1.2	The Compact Muon Solenoid (CMS) detector . . . . .	6
1.2.1	Tracker . . . . .	9
1.2.2	Electromagnetic Calorimeter (ECAL) . . . . .	11
1.2.3	Hadronic Calorimeter (HCAL) . . . . .	13
1.2.4	Solenoid . . . . .	14
1.2.5	Muon system . . . . .	16
1.2.6	Trigger system . . . . .	19
1.2.7	Data acquisition system . . . . .	21
<b>2</b>	<b>Data, signals and backgrounds</b>	<b>23</b>
2.1	The Monte Carlo (MC) simulation method . . . . .	23
2.2	Data samples . . . . .	25
2.3	Signal samples . . . . .	25
2.4	Background prediction . . . . .	25
2.4.1	The main background: $t\bar{t}$ . . . . .	25
2.4.2	Drell-Yan estimation . . . . .	25
2.4.3	Non prompt contamination . . . . .	25
2.4.4	Smaller backgrounds . . . . .	25
2.4.5	Weights and corrections applied . . . . .	25
<b>3</b>	<b>Event selection</b>	<b>27</b>
3.1	Signal regions . . . . .	27
3.2	Control regions . . . . .	27
3.3	Background-signal discrimination . . . . .	27

3.3.1	Discriminating variables . . . . .	27
3.3.2	Neural network . . . . .	27
<b>4</b>	<b>Results and interpretations</b>	<b>29</b>
4.1	Systematics and uncertainties . . . . .	29
4.2	Results . . . . .	29
<b>5</b>	<b>Conclusions</b>	<b>31</b>
5.1	Future prospects . . . . .	31
	<b>Appendices</b>	<b>33</b>
	<b>Bibliography</b>	<b>37</b>



# Chapter 1

## The experimental setup

The data analyzed throughout this work is the result of the proton-proton collisions at a center of mass energy of 13 TeV provided by the Large Hadron Collider (LHC). It is therefore extremely important to describe this particle accelerator and to detail its main characteristics in order to understand better the origin of our data, as will be done in Section 1.1.

This kind of collisions at high energy typically produces hundreds or even thousands of new particles that we then need to identify, and whose exact properties, such as their momentum or electric charge, need to be measured. This is done by using the Compact Muon Solenoid (CMS) detector, an incredibly sophisticated detector, result of the work of thousands of scientists and made of several different layers, which will be described in Section 1.2 of this chapter.

### 1.1 The LHC accelerator

The Large Hadron Collider (LHC) is a superconducting particle accelerator able to accelerate protons and heavy lead ions up to a velocity close to the speed of light. Planned since the end of the 20th century, this accelerator, a 27 kilometers ring put 100 meters underground to remove part of the contamination due to the cosmic rays and located at European Council for Nuclear Research (CERN), has now been running for 10 years. The LHC is the result of the collaboration between thousands of scientists of more than 100 different nationalities and its main objective was first of all to either infer or confirm the possible existence of the Higgs boson, theoretically predicted in the 1960s [1, 2] but never observed in any experiment. The discovery of the Higgs boson, announced at CERN on the 4th of July 2012 [3, 4], was then an incredible achievement of the accelerator, after only two years of operation.

Now that the Higgs boson has been discovered, the priority of the LHC shifted a bit. Even though many different teams are still studying this particle in order to determine precisely its most fundamental properties such as its mass or its spin, many groups of scientists are now involved in different kind of Beyond the Standard Model (BSM) physics since the LHC, whose center of mass energy has kept increasing over the years, allow us to reach a level of energy never reached before and therefore allows us to probe new parts of the phase space, searching for eventual hints of new physics. These kind of searches of course include the search for eventual Dark Matter (DM) production as the one performed in this work.

Let's now start with a global description of the general design of this particle accelerator in Section 1.1.1 before describing in more details the key parameters allowing us to evaluate its actual performances in Section 1.1.2.

### 1.1.1 The LHC in a nutshell

The LHC is an underground particle accelerator built in the same 27 kilometers tunnel where the Large Electron Positron collider (LEP) was previously used. This machine is accelerating two beams made out of billions of protons or lead ions in each direction and is mostly made out of more than 4000 superconducting magnets, in majority dipoles and quadrupoles, allowing respectively to curve the beam to maintain a nominal circular trajectory and to focus it by compensating its natural dispersion due to the repulsion of the protons making up these beams. A dedicated small section of the accelerator is then made out of 16 radio-frequency cavities synchronized in such a way that these protons always face a negative electric charge, which is used as the driving process of the actual acceleration of such particles.

Once the nominal center of mass energy  $\sqrt{s} = 13$  TeV reached (this concept will be described in Subsection 1.1.2), the protons are then smashed together in four different places on the LHC, where the four detectors (A Toroidal LHC ApparatuS (ATLAS), CMS, A Large Ion Collider Experiment (ALICE) and LHCb) have been placed in order to study the collisions. Both ATLAS and CMS are general detectors able to study exotic processes such as the production of DM and to make precision measurements on Standard Model (SM) physics as well (the decision to build two separate detectors was made in order to introduce some redundancy and to check the results). ALICE on the other hand is mostly dedicated to the study of heavy ions collisions that happen  $\sim 10\%$  of the time in order to study in particular a specific state of matter, called the quark-gluon plasma [80]. Finally, LHCb has been designed to study in particular the CP violation phenomena, which could be the sign of some new physics [81].

It is important to note at this point that the LHC is not a standalone accelerator in the sense that protons enter the LHC with a velocity already close to the speed of light. In order to reach such input energies ( $\sim 450$  GeV), previous smaller accelerators of CERN are still used today. A chain of accelerators is then formed: first of all, the protons, extracted from a bottle of ordinary hydrogen, are injected into the LINAC 2, a linear accelerator, before being transferred to the Proton Synchrotron (PS), the Super Proton Synchrotron (SPS) and finally the LHC itself (all this chain of acceleration can be found in Figure 1.1).

During this phase of acceleration, the beam is separated in 2808 bunches of protons nominally separated by 25ns (giving a collision rate of 40 MHz), so that the experiments have the time to record the collision, clean the detectors and get ready for the next bunch crossing, coming just a few nanoseconds later. Each time one bunch crossing happens, around 35 collisions of protons happen at once: this phenomena, usually referred to as Pile Up (PU), has to be taken into account as well and will be described in the next section.

As previously stated, the amount of data collected is a crucial parameter for many analyses, meaning that the LHC would ideally need to run 24 hours a day, 365 days per year in order to

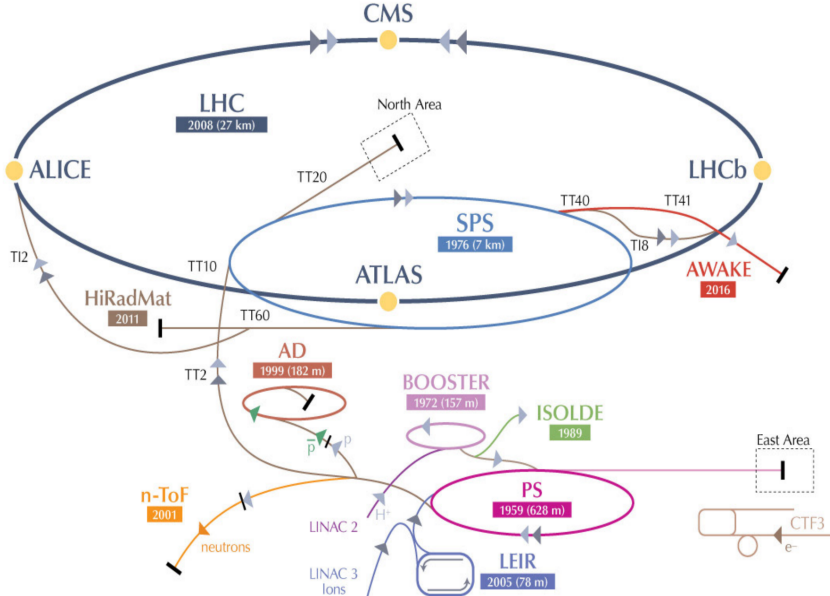


Figure 1.1: LHC injection chain and experiments performed at CERN [83].

maximize the data taking. However, this is not possible, as setting up a beam takes time and cannot keep rotating at maximal energy in the machine for a long time, so in ideal conditions around 20 hours of data taking a day are expected. The LHC is then running around 9 months per year, being usually stopped during the winter for maintenance operations, and the data taking periods are defined into Runs of a few years, after which the accelerator is usually stopped for a longer period of time, a Long Shutdown (LS), in order to also have the time to perform upgrade operations of the machine.

The data analyzed in this work corresponds to the second phase of the Run II of operation of the LHC, from 2016 to 2018, while the Run III is now expected to start in the Spring of 2021. The summary of the main parameters of operation of the LHC across the different Runs of operations can be found in Table 1.1.

### 1.1.2 LHC key parameters

#### Center of mass energy

The center of mass energy is defined as a Lorentz invariant quantity under longitudinal boosts resulting of the collisions of two protons (defined as  $E_1, \vec{p}_1, m_1$  and  $E_2, \vec{p}_2, m_2$ ) with a  $\theta$  angle, as developed in Equation 1.1. It is a key variable of the LHC since the phase space of particles that can be explored directly depend on this value.

$$\sqrt{s} = \sqrt{(m_1)^2 + (m_2)^2 + 2(E_1 E_2 - 2|\vec{p}_1| |\vec{p}_2| \cos(\theta))} = 13 \text{ TeV} \quad (1.1)$$

The LHC started its operation in 2008 running at an energy of 7 TeV, quickly moved to 8 TeV

Parameter	Run I	Run II	Run III	Design
Energy [TeV]	7 → 8	13	14	14
Bunch spacing [ns]	50	25	25	25
Intensity [ $10^{11}$ ppb]	1.6	1.2	Up to 1.8	1.15
Bunches	1400	2500	2800	2800
Emittance [ $\mu\text{m}$ ]	2.2	2.2	2.5	3.5
$\beta^*$ [cm]	80	30→25	30 → 25	55
Crossing angle [ $\mu\text{rad}$ ]	-	300 → 260	300 → 260	285
Peak luminosity [ $10^{34} \text{ cm}^{-2} \text{ s}^{-1}$ ]	0.8	2.0	2.0	1.0
Peak PU	45	60	55	25

Table 1.1: Expected and observed main parameters of  $pp$  operation of the LHC across the different eras of operation [82].

and kept this level of energy during the end of the Run I of operation. In 2015, for the Run II of data taking, the energy was increased until reaching 13 TeV (2 times 6.5 TeV for each beam) and an expected value of 14 TeV, the nominal energy for which the LHC was originally built, is expected to be reached in the near future.

## Luminosity

The luminosity is another extremely important variable for the operation of the LHC since, as a rule of thumb, it gives an indication on the number of collisions per second given by the accelerator. Increasing this parameter is then crucial to collect as much data as possible, in order to be able to isolate processes having a low production cross section and therefore an extremely low probability of apparition when colliding two protons.

Mathematically, we can first of all define in Equation 1.2 the rate  $R$  of production (in number of events per second) of any given process using its cross section  $\sigma$ , equivalent to its production probability, and the instantaneous luminosity  $\mathcal{L}$ . From this rate can be extracted easily the number of expected interactions  $N$  in a certain amount of time  $T$  as well.

$$\begin{cases} R = \mathcal{L} \cdot \sigma \\ N(T) = \sigma \int_0^T \mathcal{L}(t) dt = \sigma L \end{cases} \quad (1.2)$$

This instantaneous luminosity we just introduced  $\mathcal{L}$  can be defined using Equation 1.3, assuming that the beams have a Gaussian profile, while the integrated luminosity  $L$  can be defined by simply integrating the instantaneous luminosity over time  $L = \int \mathcal{L} dt$  [84].

$$\mathcal{L} = \frac{\gamma f_{\text{rev}} k_B N_p^2}{4\pi \epsilon_n \beta^*} R \text{ where } R = \frac{1}{\sqrt{1 + \frac{\theta_C \sigma_z}{2\sigma}}} \quad (1.3)$$

In this last equation, the following properties of the accelerator have been introduced, giving the LHC a nominal instantaneous luminosity  $\mathcal{L} = 10^{34} \text{ cm}^{-2} \text{ s}^{-1}$ :

- $\gamma$  is the usual relativistic Lorentz factor (for the LHC, when protons go at their maximum velocity of 99.9999991% of the speed of light,  $\gamma = 7460$ )
- $f_{\text{rev}}$  is the frequency of revolution (11.2 kHz)
- $k_B$  is the number of proton bunches per beam (2808 for a 25 ns bunch spacing)
- $N_p$  is the number of protons per bunch ( $1.15 \cdot 10^{11}$  protons)
- $\epsilon_n$  is the transverse normalized emittance ( $3.75 \mu\text{m}$ )
- $\beta^*$  is the betatron function at the interaction point (0.55 m)
- $R$  is the geometrical factor accounting for the fact that the collisions do not happen exactly head-on, therefore reducing the effective luminosity, expressed from the full crossing angle between colliding beam  $\theta_C$  (285  $\mu\text{rad}$ ), and  $\sigma, \sigma_z$ , the transverse and longitudinal r.m.s. sizes (respectively 16.7  $\mu\text{m}$  and 7.55 cm).

As previously stated, increasing the luminosity of the LHC is always something interesting in order to produce processes having a low production cross-section, and we can then see that many different parameters can be tweaked in order to achieve the highest possible instantaneous luminosity, such as the number of protons per bunch, the number of bunches per beam or the beam crossing angle at the interaction point. New crab cavities will probably be installed during the next LS of the LHC in order to increase the value of the geometrical factor  $R$  and the instantaneous luminosity by a factor  $\sim 10$  (HL-LHC project [85]).

The total integrated luminosity taken by the LHC during its different years of operation has been summarized in Figure 1.2. The final datasets available and analyzed in this work have an integrated luminosity of  $35.9 \text{ fb}^{-1}$  (2016),  $41.5 \text{ fb}^{-1}$  and  $59.7 \text{ fb}^{-1}$  (2018), resulting in a total dataset of  $137 \text{ fb}^{-1}$  recorded during the Run II of operation. This means that we roughly expect to produce around 137 events of any process whose cross section of production would be equal to 1  $\text{fb}$ .

## Pile Up (PU)

The last key parameter of the LHC discussed here is the Pile Up (PU). Usually, because of the high density of protons within the beams, a bunch crossing in a experiment produces around 35 collisions protons collisions, as seen in Figure 1.3, of which only the most interesting one will be kept, defining the Primary Vertex (PV), while the other vertices are usually referred to as the PU. The tracker of CMS, which will be introduced in Section 1.2.1, therefore needs to be able to reconstruct all these events in order to define the PV of the interaction.

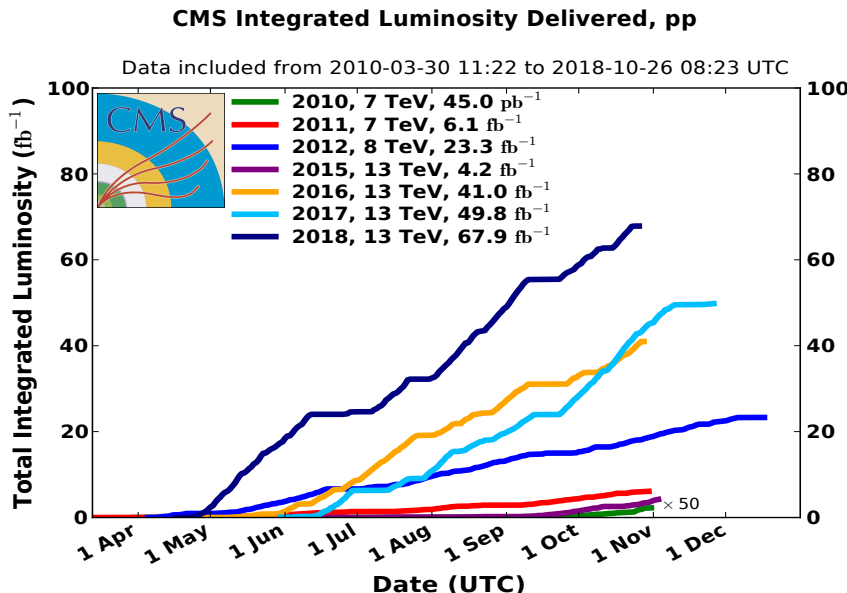


Figure 1.2: Integrated luminosity collected by CMS over its different years of operation so far.

## 1.2 The CMS detector

The Compact Muon Solenoid (CMS) is one of the two general purpose detectors installed at the access point 5 of the LHC. Its main purposes were to discover the Higgs boson, make precision measurement of most of the SM processes and to try and discover BSM physics, such as the possible existence of DM.

It has been carefully designed by hundreds of different physicists and engineers in order to be as hermetic as possible, covering all the possible angles around the beam pipe, the point of origin of all the collisions provided by the LHC, and is therefore made of three main sections: the cylindrical barrel at the center, and the two endcaps, one on each side of the detector. CMS, quite compact with its 14.000 tons, diameter of 15 meters and length of 28.7 meters, was lowered into the experimental cavern after being built on the surface in 14 different moving pieces, a flexible design allowing to access its inner parts, by opening and closing the detector when needed.

### Main goals

The CMS detector has been built in order to meet the goals of the LHC physics program, which have been summarized in [86] as:

- Good muon identification and momentum resolution over a wide range of momenta and angles, good dimuon mass resolution ( $\sim 1\%$  at 100 GeV), and the ability to determine unambiguously the charge of muons with  $p < 1$  TeV.
- Good charged-particle momentum resolution and reconstruction efficiency in the inner tracker. Efficient triggering and offline tagging of taus and b-jets, requiring pixel detectors close to

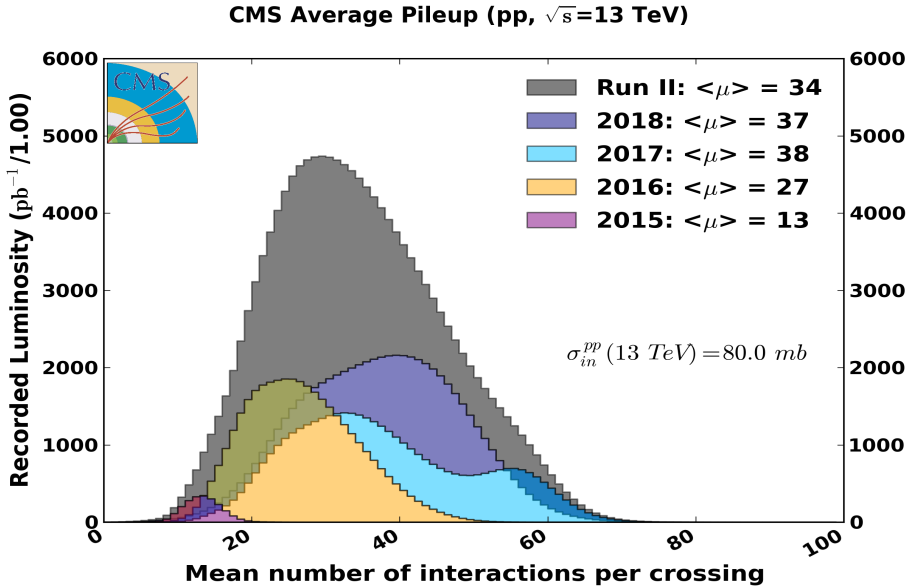


Figure 1.3: Mean PU distribution and luminosity recorded by CMS over the different years of operation of the LHC.

the interaction region.

- Good electromagnetic energy resolution, good diphoton and dielectron mass resolution ( $\sim 1\%$  at 100 GeV), wide geometric coverage,  $\pi^0$  rejection, and efficient photon and lepton isolation at high luminosities.
- Good missing-transverse-energy and dijet-mass resolution, requiring hadron calorimeters with a large hermetic geometric coverage and with fine lateral segmentation.

### CMS subdetectors

As shown in Figure 1.4, CMS is made out of different layers corresponding to different subdetectors, each able to provide different kind of information about the particles created by each collision [86]. These subdetectors will be described in details in the following sections, but they have all been designed in order to make the reconstruction of the different events as efficient, fast and precise as possible and need to be quite cheap but still extremely resistant to the radiation produced.

The inner part of the CMS detector is the so-called tracker, a device made out of silicon pixels and strips, described in Section 1.2.1 and responsible for the precise reconstruction of all the charged particles coming from the different interaction vertices. A bit further outside can be found the Electromagnetic Calorimeter (ECAL), made out of thousands of crystals as described in Section 1.2.2 and used to precisely measure the energy of particles able to interact electromagnetically by producing an electromagnetic shower that can be detected. Then comes the Hadronic Calorimeter (HCAL), described in Section 1.2.3 and whose main purpose is to identify and measure the main properties of the hadrons produced in the collisions by producing hadronic showers.

The CMS name partly comes from its central piece, a huge superconducting solenoid described

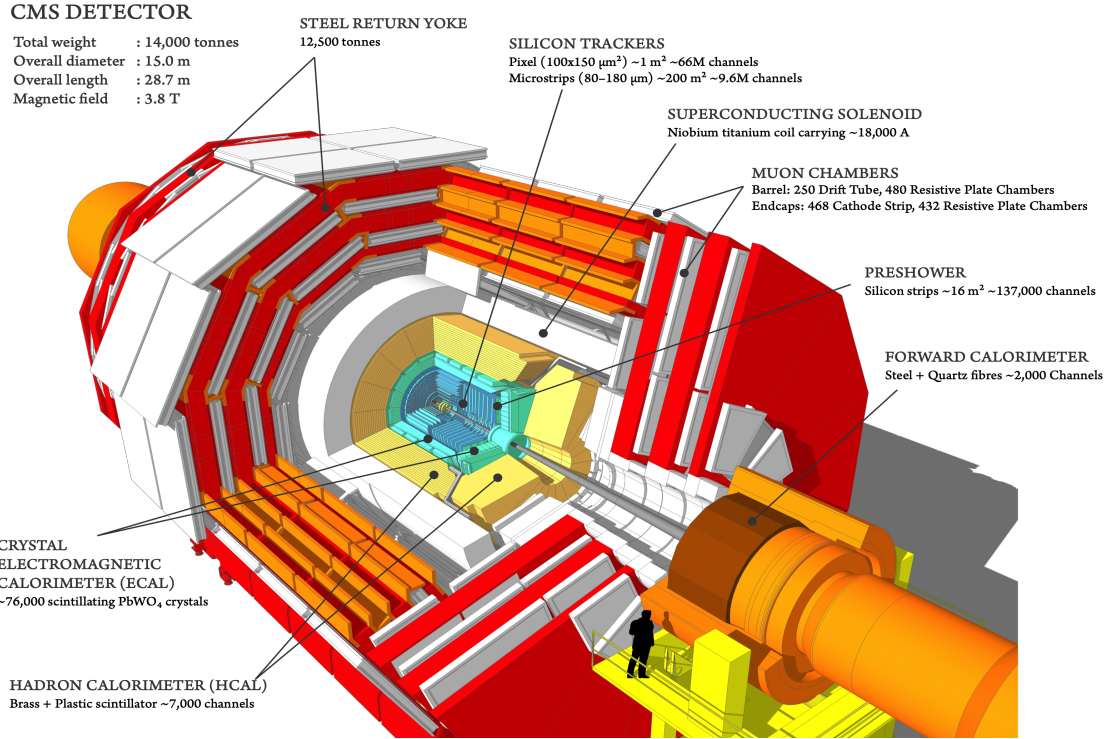


Figure 1.4: Schematic representation of the CMS detector, along with all its subdetectors and main characteristics.

in Section 1.2.4 and able to produce a 3.8 T magnetic field in the detector, with a magnetic flux density increased even more by the addition of the steel return yoke layers (red parts in Figure 1.4). This magnetic field is essential in the sense that it is able to deflect the charged particles which have been produced via the Lorentz interaction, therefore giving us an additional way to measure their charge and energy from the measurement of the curvature of the induced binding.

Finally, on the outside of the detector can be found the complete muon system and particularly performing in CMS. This subdetector is currently made out of three main sub-systems (the Drift tubes (DTs), Cathode Strip Chambers (CSCs) and Resistive Plate Chambers (RPCs)), as explained in Section 1.2.5, and is responsible for the identification and measurement of the momentum of the muons produced by the collisions.

### Coordinate system

Before starting with the description of all these subdetectors, it is important to detail the coordinate system typically used within the CMS collaboration. As a convention, it has been decided to use a right-handed Cartesian coordinate system with the origin defined as the Primary Vertex (PV), and with an x-axis pointing towards the center of the ring, an y-axis pointing upwards and a z-axis pointing towards the Jura mountains (along the counterclockwise beam direction), as represented in Figure 1.5.

The  $\theta$  and  $\phi$  angles are then defined as the angles between the z and y axes and the x and y axes respectively and the pseudorapidity  $\eta$ , defined in Equation 1.4, a Lorentz invariant quantity under

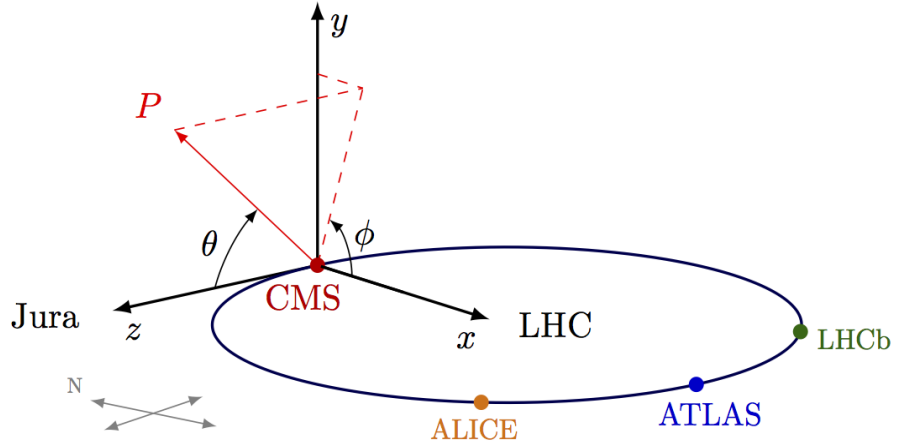


Figure 1.5: Schematic representation of the CMS coordinate system used by convention.

longitudinal boosts quite often used in the different analyses since the multiplicity of high energy particles is roughly constant in  $\eta$ .

$$\eta = -\log \left( \tan \left( \frac{\theta}{2} \right) \right) \quad (1.4)$$

### 1.2.1 Tracker

The tracker is the innermost part of the CMS detector, is 5.4 meters long and has a diameter of 2.5 meters. Its main purpose is the reconstruction of the trajectories of charged particles issued from the primary and secondary interaction vertices in a quick and precise way in order to identify them and measure their individual momentum.

Many challenges were faced when designing this system mainly because of the hard conditions provided by the LHC. First of all, at its nominal instantaneous luminosity, an average of 1000 particles are created after each bunch crossing, every 25 nanoseconds. The tracking system then needs to read all its channels extremely fast in order to be ready for the next bunch crossing. However, this fast electronics then needs some cooling to work optimally, which would in return increase the size of the tracker and therefore increase the interactions between the detector and the particles created (by multiple scattering, bremsstrahlung, photon conversion and nuclear interactions). This would affect the trajectory of the particles so a compromise had to be found between the velocity and size of the tracker. Finally, this device needs to be resistant to the extreme radiation environment for its expected lifetime of at least 10 years.

This device is then made out of silicon pixels and strips mainly because of the granularity, reading velocity and radiation hardness offered by such material. It has been set up on several different layers disposed in such a way to make the detector as hermetic as possible, as shown in Figure 1.6. A charged particle crossing the tracker will then leave a hit each time it crosses one of the silicon sensor, from which the track of the particle can be reconstructed using performing reconstruction algorithms that will be detailed in Chapter ??.

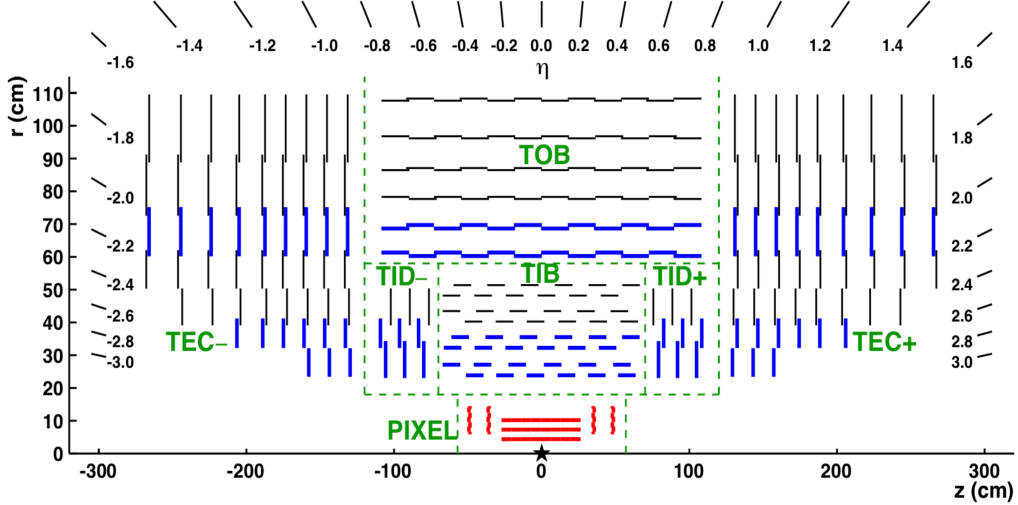


Figure 1.6: Schematic representation of the CMS tracker, for different pseudorapidity values and along the z-axis [87].

The presence of the magnetic field due to the solenoid can then help us estimate the momentum of the particle, since the Lorentz force applied on such particle will introduce a deviation directly proportional to its momentum. The radius of curvature of particles with a high momentum ( $> 100$  GeV) is really large but the density of pixels and the algorithm can still manage to estimate the momentum of such particles, even though the uncertainty associated will then be greater.

In particular, the tracker is made out of two distinct parts: the smaller and inner pixel detector and the larger silicon strip detector:

- The **pixel detector** is made out of three barrel pixel layers and two endcap disks for hermeticity (located at  $r = 4.4, 7.3$  and  $10.2$  cm of the PV), one on each side. In total, more than 60 millions pixels make up this detector, covering an area corresponding to  $\sim 1 \text{ m}^2$ .
- The **silicon strip detector** on the other hand is composed of three different sub-systems, as seen in Figure 1.6 and covers a total area of  $\sim 200 \text{ m}^2$ . First of all, the Tracker Inner Barrel and Disks (TIB/TBD) add an additional 4 barrel layers and 3 endcap disks to the tracker system up to a distance  $r = 55$  cm to the PV of the interaction, using silicon micro-strip sensors parallel in the barrel and perpendicular to the beam axis in both endcaps. Then, the Tracker Outer Barrel (TOB) surrounds this first layer; having an outer radius of 166 cm and going up to 118 cm along the z-axis, it adds 6 layers to the inner tracking system. Finally, the Tracker EndCaps (TECs) are made out of 9 disks and complete the measurement of particles emitted along the z-axis and having a high pseudorapidity  $\eta$ .

The CMS tracker is extremely performing: we can see in Figure 1.7 that muons are indeed reconstructed with an efficiency higher than 99% for most of the pseudorapidity spectrum, even though we can observe that this efficiency drops at high  $\eta$  values mainly because of the reduced coverage provided by the pixel forward disks. The interactions between the hadrons and the tracking system is also a bit higher, which result in a lower reconstruction efficiency for such particles.

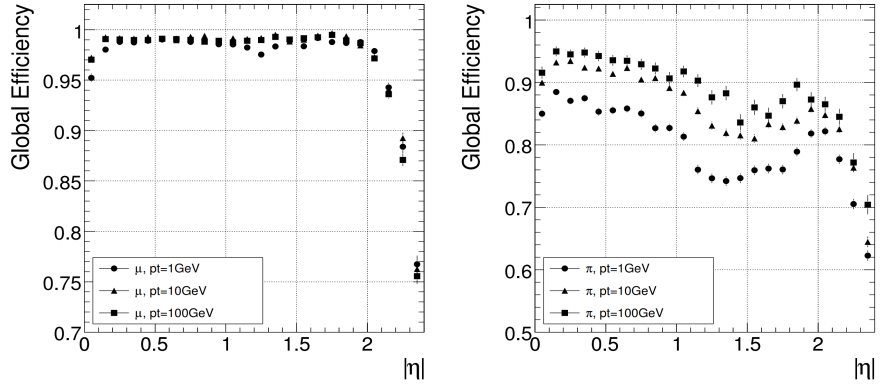


Figure 1.7: Tracker reconstruction efficiency of muons (on the left) and pions (on the right) for different pseudorapidities and particle momenta (1, 10 and 100 GeV) [86].

### 1.2.2 Electromagnetic Calorimeter (ECAL)

The Electromagnetic Calorimeter (ECAL) of CMS is a mostly homogeneous detector inside the solenoid but enclosing the tracker system that gives information about the energy of electrons and photons, both able to interact electromagnetically with its crystals.

The ECAL can also be divided into several sections: first of all, at pseudorapidities  $|\eta| < 1.479$  is found the barrel part of the ECAL (EB), made out of 61 200 lead tungstate ( $\text{PbWO}_4$ ) crystals, located at a radius of 1.29 meters of the beam pipe. Then, two endcaps, each made out of 7 324 of those crystals, increase the coverage of the detector up to  $|\eta| < 3$ , as shown in Figure 1.8, and the preshower completes the ECAL..

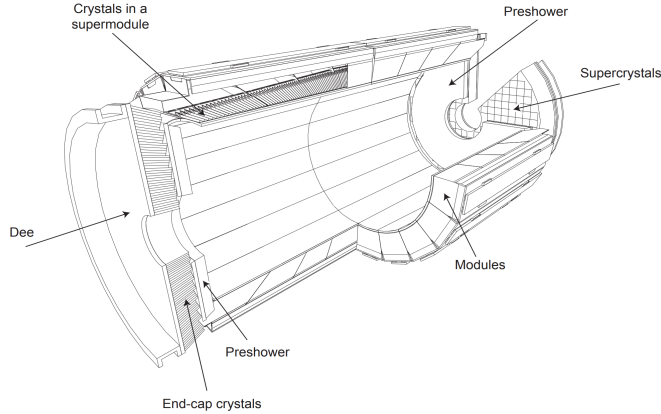


Figure 1.8: Schematic representation of the sub-systems of the CMS ECAL [86].

Its principle of action is simple and based on electromagnetic showers: when a particle such as an electron or a photon enters the ECAL, it will start to interact in different ways, depending on its nature. Photons will mainly produce pairs of electrons and anti-electrons, while the electrons themselves tend to emit additional photons by bremsstrahlung effect. This results in a chain reaction during which the incident particle will give most of its energy to the detector itself, energy

measurable using photodetectors and photomultipliers. This effect is known as an electromagnetic shower, is represented in Figure 1.9 and is usually characterized using the so-called radiation length  $X_0$ , the mean distance over which a high-energy electron loses all but  $1/e$  of its energy, then determining the total length of interaction of a particle in the ECAL.

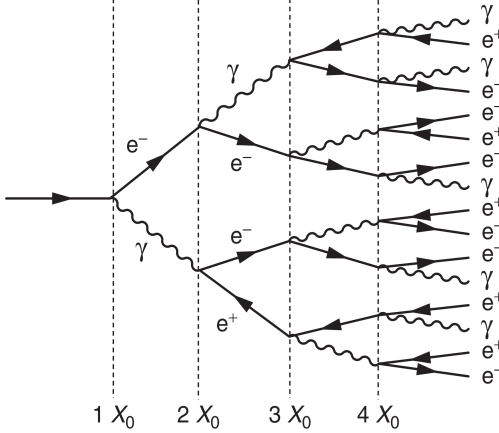


Figure 1.9: Schematic representation of a typical electromagnetic shower and the radiation length  $X_0$  concept [86].

The high density, short radiation length and low scintillation decay time (smaller than the bunch spacing of 25ns) of the PbWO<sub>4</sub> crystals make them perfect candidates towards a compact ECAL in CMS. These crystals do have some drawbacks as well, mainly their relative fragility when it comes to radiation, and the dependence on the temperature of their response. Indeed, a cooling system had to be built in order to keep the huge detector under temperature variations lower than 0.1° to avoid eventual fluctuations in the response of the crystals.

These crystals, which had to be grown individually in laboratories, measure 2.2x2.2x23cm in the barrel and 3x3x22cm in the endcaps, cover a solid angle equal to  $(\Delta\eta, \Delta\phi) = (0.0174, 0.0174)$ , and have therefore a length corresponding to around 26 radiation lengths, more than enough to stop even the most energetic particles. Since the light output of such crystals is quite low (only around 4.5 photoelectrons per MeV of energy), they have to be connected to both avalanche photodiodes and vacuum phototriodes in order to multiply the signal measured. Finally, they have been mounted used a specific installation, slightly tilted with respect to both  $\phi$  and  $\eta$  in order to remove any possible gap between two adjacent crystals.

The typical energy resolution of the ECAL installed at CMS is given by Equation 1.5 [86], accounting for several different effects, such as the stochastic nature of the observe scintillation, the electronics and PU noise and the calibration and detector non-uniformity uncertainty.

$$\frac{\sigma_E}{E} = \sqrt{\left(\frac{2.8\%}{\sqrt{E}}\right)^2 + \left(\frac{0.12\%}{E}\right)^2 + (0.30\%)^2} \sim \frac{3 - 10\%}{\sqrt{E/\text{GeV}}} \quad (1.5)$$

Finally, a preshower layer has been set up in the fiducial region ( $1.653 < |\eta| < 2.6$ ) of the endcaps, where the angle between the two photons coming from the decay of neutral pions  $\pi^0 \rightarrow \gamma\gamma$  is small enough to be misidentified as individual photons. This detector has then been installed in order to

reduce the possible misidentification of such events and to help with the identification of electrons against minimum ionizing particles. It is made of a lead layer able to initiate the electromagnetic shower process, followed by two layers of silicon strips for the actual measurement.

### 1.2.3 Hadronic Calorimeter (HCAL)

We know that charged hadrons do lose energy in a continuous when they traverse matter due to the ionization process and that all the hadrons strongly interact with the nuclei of any given medium. These principles are actually used in order to measure the energy of the hadrons produced by the LHC collisions using the Hadronic Calorimeter (HCAL) sub-system of CMS.

In this case as well, showers of particles due to a chain reaction are expected since the primary hadronic interaction will produce several additional hadrons, themselves interacting even more with the medium while losing energy. This kind of hadronic showers is characterized by the  $\lambda$  parameter, the nuclear interaction length, defined as the mean distance between two interactions of relativistic hadrons. The nuclear interaction length  $\lambda$  is usually much larger than the radiation length  $X_0$ , resulting in a HCAL typically much larger in size than the ECAL.

A typical HCAL setup consists in alternating thick and high-density layers of absorber material, in which the showers can develop, and thin layers of active material used for the actual detection by sampling the energy deposition. This measurement is usually much less precise than the measurement provided by the ECAL, mostly since  $\pi^0$  decaying into photons can appear in these showers, leading to an electromagnetic component of the shower that cannot be measured, and because around 30% of the incident energy is usually lost due to nuclear excitation and break-up effects [84]. In this case, the energy resolution can therefore be expressed using Equation 1.6.

$$\frac{\sigma_E}{E} > \frac{50\%}{\sqrt{E/\text{GeV}}} \quad (1.6)$$

In CMS, the HCAL, represented in Figure 1.10, is also divided into a barrel (HB), radially constrained between radii values of 1.77 meters (outer radius of the ECAL) and 2.95 meters (inner radius of the solenoid), and two symmetrical forward regions (HF) extending the pseudorapidities coverage from  $|\eta| = 3$  to  $|\eta| = 5.2$  and located at a distance of 11.2 meters to the PV. A final part composing the HCAL is the so-called Hadron Outer (HO), which has to be put outside of the solenoid in order to increase the amount of shower absorber material of the HCAL and therefore the effective nuclear radiation length  $\lambda$ .

The HCAL barrel uses 36 identical azimuthal wedges as absorber, placed along the beam axis in such a way that the eventual cracks between them is smaller than 2 mm. The total absorber thickness at a  $90^\circ$  incidence angle is equal to only  $5.8\lambda$ , which explains why the HO had to be added in order to increase this value to make sure to slow down and completely stop even the most energetic hadrons. The active medium of the HB is made out of 70 000 tiles able to collect the scintillation light, using the wavelength shifting fibre concept to measure the energy of the hadrons. The HF on the other hand are using a Cerenkov-based radiation-hard technology to make the measurements required.



Figure 1.10: Schematic representation of the HCAL sub-system in CMS [86].

The barrel covers  $|\eta|$  regions up to 1.3, while the coverage up to  $|\eta| < 5.2$  is given by two endcaps on each side of the detector, placed in such a way to minimize the eventual cracks between the HB and the two HF. Finally, the HO, built in order to ensure adequate sampling depth at low pseudorapidities values, actually uses the solenoid itself as additional absorber material, since it is placed a bit outside of this coil. Its shape is constrained by the muon system and the mean fraction of recovered energy from the HO has been estimated to be equal to 0.38% for 10 GeV pions and up to 4.3% for 300 GeV pions, as shown in Figure 1.11.

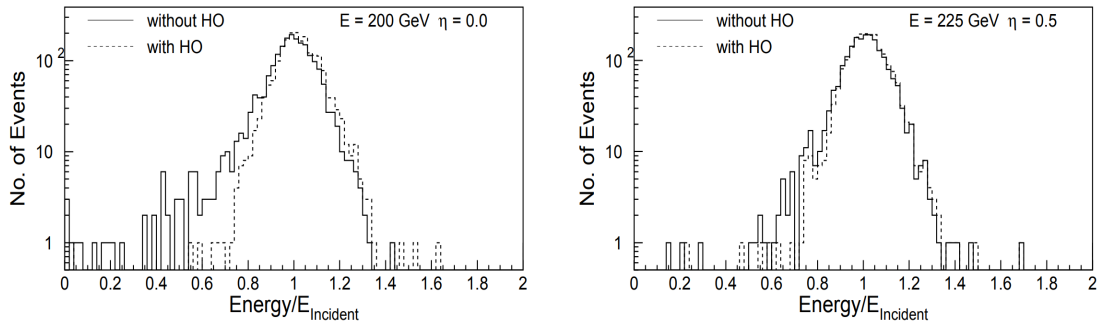


Figure 1.11: Distribution of the measured energy scaled to the incident energy for pions with incident energies of 200 GeV at  $\eta = 0$  (on the left) and 225 GeV at  $\eta = 0.5$  (on the right), with and without the inclusion of the HO in the HCAL system [86].

#### 1.2.4 Solenoid

The central piece of CMS is its extremely large (12.5 meters of length and 6 meters of diameter) and heavy (220 tons) superconducting solenoid able to produce a 3.8T magnetic field, storing when active a huge energy of 2.6 GJ. It is the largest magnet of its type ever constructed, therefore

allowing the tracker, ECAL and HCAL calorimeters to be placed inside the coil, resulting in a detector that is, overall, quite compact compared to detectors of similar weight.

The magnetic field produced by this coil is extremely useful since it allows to measure quite precisely the charge and the momentum of the different charged particles interacting with the detector just by measuring the curvature of their track, according to the Lorentz equation 1.7. This solenoid has been designed to reach a momentum resolution  $\Delta p/p \sim 10\%$  at  $p = 1$  TeV.

$$\vec{F} = \frac{m \vec{v}^2}{R} = q \vec{E} + q \vec{v} \times \vec{B} = q \vec{v} \times \vec{B} \quad (1.7)$$

The hoop strain  $\epsilon = 130$  MPa applied throughout this solenoid is quite large compared to the strain applied on other previous detectors and this had to be taken into account during the conception of this magnet. It has then been designed in such a way that a large fraction of the CMS coil has a structural function, dividing the strain between the layers of the magnet and the support of the coil itself ( $\sim 30\%$ ). At the end, the conductor of this solenoid, made from a Rutherford-type cable combined with aluminium, is mechanically reinforced with an aluminium alloy.

The coil of the magnet is then completed with a huge steel yoke return system, as seen in Figure 1.12, made out of 6 endcap disks and 5 barrel wheels, weighting in total more than 12 000 tons and therefore accounting for most of the weight of CMS. This system is composed of many steel blocks up to 620 mm thick combined and actually also serves as the absorber plates of the HO and muon detection system that will be described in the next section.



Figure 1.12: Picture of the solenoid system of CMS being setup in the assembly hall.

Finally, a two pumping stations system has been put in place in order to setup a vacuum as strong as possible inside the  $40 \text{ m}^3$  volume of the coil cryostat and an helium refrigeration plant has been installed near the site of the detector, able to cool down the solenoid up to 4.5 K, giving a 2 K security margin with respect to the critical field of the superconducting coil. All these systems were extensively tested on the surface during the summer of 2006, before lowering down the complete solenoid in the experimental cavern where it now stands.

### 1.2.5 Muon system

The muon detection in a detector is extremely useful since many interesting processes are expected to produce such particles. Their detection and the correct measurement of their main properties such as their position and momentum is therefore crucial in most of the analyses performed. Detecting muons is at the end of the day quite easy, as we will see, and the data extracted from them is usually more reliable than the one obtained from electrons since muons are less likely to be affected by the inner parts of the detector, such as the tracker, because of their low interaction cross section with usual matter.

The muon system of CMS is actually made out of three different gaseous sub-subsystems combined in order to perform a reconstruction as precise as possible of such particles over the entire kinematic range of the LHC. These different muon chambers systems do share some characteristics: they mostly have to be cylindrical, because of the geometrical shape of the inner systems of CMS and they have to be reliable and cheap, since they cover a total area of more than  $25\,000\text{m}^2$ .

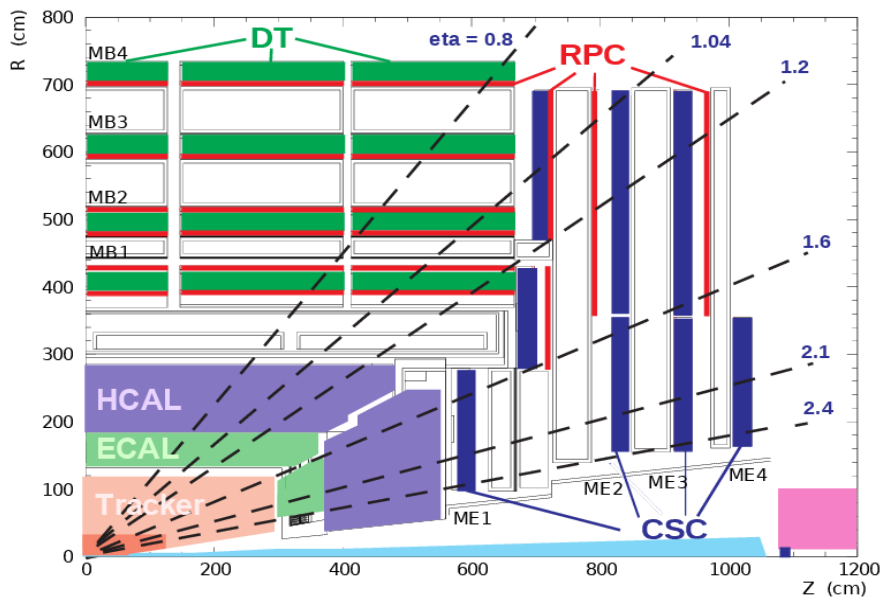


Figure 1.13: Geometrical repartition along the z-axis of the different muon chambers in CMS [88].

Let's now describe in details each category of muon chambers used in the different pseudorapidities areas, as shown in Figure 1.13, in order to form as muon system as hermetic as possible.

#### Drift tubes (DTs)

First of all, in the barrel region, where the flux of muons is low and where the magnetic field is mostly uniform and low as well, the **Drift tubes (DTs)** have been installed. This system covers the  $|\eta| < 1.2$  area and has been divided into 4 different layers, each containing a number of stations optimized in order to provide a full coverage of the  $\theta$  angles, a good efficiency for the muon hits reconstruction into a single track and a good rejection of eventual background hits. This distribution of the DTs is represented in Figure 1.14.

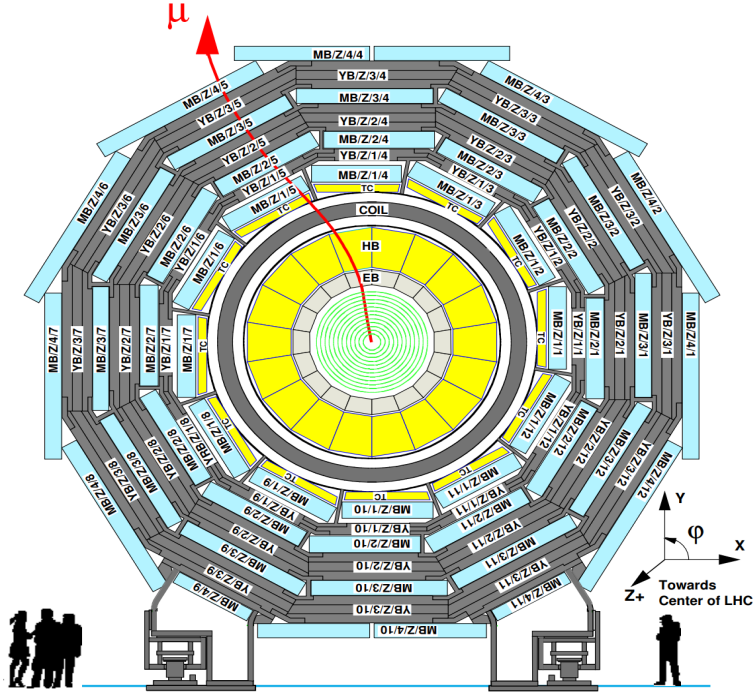


Figure 1.14: Lateral geometrical division of the different DT chambers in one of the 5 wheels of CMS [86].

The DT system is made out of 172 000 sensitive wires able to collect the residuals charges left by the ionization tracks of muons through the 250 chambers installed. The system has been set up in such a way that the maximal drift of any charge is lower than 21mm, corresponding to a drift time of 380ns in the gaseous chambers made out of 85% of Ar and 15% of CO<sub>2</sub>, a value small enough to produce negligible occupancy in the different wires and to avoid the need of multi-hits electronics. Redundancy of the DTs provided by the installation of multiple layers is extremely important, mainly to reduce the backgrounds coming from eventual neutrons or photons, whose rate is actually much larger than the one obtained from prompt muons.

### Cathode Strip Chambers (CSCs)

In the two endcap regions, where the muon rates and the background levels are much larger and where the magnetic field is large and non-uniform, a different system had to be installed. First of all, the **Cathode Strip Chambers (CSCs)**, multiwire proportional chambers providing a fast response while being resistant to the radiation, are able to identify muons in a  $0.9 < |\eta| < 2.4$  region (in the  $0.9 < |\eta| < 1.2$  region, muons cross both DTs and CSCs while in the  $1.2 < |\eta| < 2.4$  area, muons cross between 3 and 4 CSCs only).

This sub-system is made out of 540 different chambers in total, all perpendicular to the beam pipe. The sensitive plates of this sub-system are made out of 2 million wires, cover about 5000m<sup>2</sup> and the total gas volume included in such chambers is equal to about 50m<sup>3</sup>.

## Resistive Plate Chambers (RPCs)

Finally, some **Resistive Plate Chambers (RPCs)** have been added to the barrel and to the endcap regions in order to cope with the uncertainty associated with the eventual background rates and with the (in)ability of the previous muon system to identify unequivocally the correct bunch crossing when the LHC is running at full luminosity. Indeed, the time resolution of the DTs of 380ns is way larger than the bunch spacing in the LHC, while a RPC is capable of tagging an ionizing event in less than 25ns, make it an ideal candidate to trigger the event.

The RPCs are double-gap chambers operated in avalanche mode to ensure good operation at high rates and they are able to produce a fast response with good time resolution, even though its position resolution is worse than the one obtained with DTs or CSCs. The RPCs are also useful in the sense that they can help to resolve ambiguities when attempting to construct tracks from multiple hits in a chamber.

Finally, the different features of the three muon sub-systems used by the CMS detector and just described are summarized in Table 1.2.

Muon sub-system	DT	CSC	RPC
$ \eta $ coverage	0.0-1.2	0.9-2.4	0.0-1.9
Stations	4	4	4
Chambers	250	540	480 (barrel) 576 (endcaps)
Readout channels	172 000	266 112 (strips) 210 816 (anode channels)	68 136 (barrel) 55 296 (endcaps)

Table 1.2: Comparison of the three main sub-systems currently used by CMS in order to identify muons [89].

Another advantage of the muon system such as the one built in CMS is that it can also directly be used by the trigger system, which will be described in Section 1.2.6, independently of the rest of the detector and in addition of being able to detect, identify and measure several properties of muons crossing it.

The muon reconstruction efficiency obtained by the muon system strongly depends on the pseudorapidity value of the muon considered, along with its transverse momentum, as shown in Figure 1.15. In this figure, we can also see that several different kinds of muons can be defined, such as the **standalone muons**, defined using only the data coming the muon system and the **global muons**, defined using both the information coming from the muon system and the tracker. This distinction will be detailed when discussing about the muons reconstruction in Section ??).

Taking advantage of the Long Shutdown (LS) 2, a new muon system is currently being installed in the experimental cavern: the so-called **Gas Electron Multipliers (GEMs)**, placed in the endcaps, where the radiation and event rates are the highest. This new subdetector will provide additional redundancy and measurement points to the current system, therefore allowing a better muon track identification and reconstruction and a wider coverage in the very forward region.

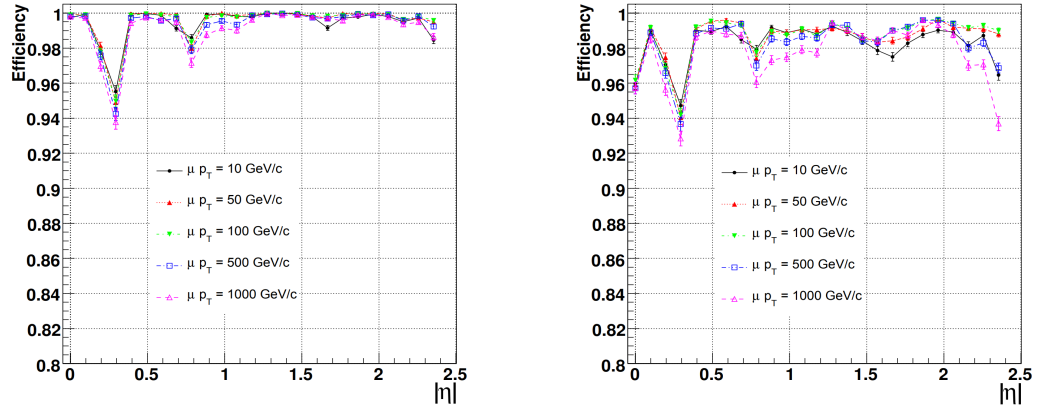


Figure 1.15: Muon reconstruction efficiency with different  $p_T$  and  $\eta$  values, considering only the muon system (on the left), and the combined information from the muon system and the tracker (on the right) [86].

The first 144 chambers of the GEM sub-system, filled with a mixture of Ar and CO<sub>2</sub> and where the primary ionization due to incident muon is expected to happen, are currently being installed in the first disk of both endcaps (cf. Figure 1.16), while the rest will be set up during the next LS expected in 2024, before the phase II of operation of the LHC.

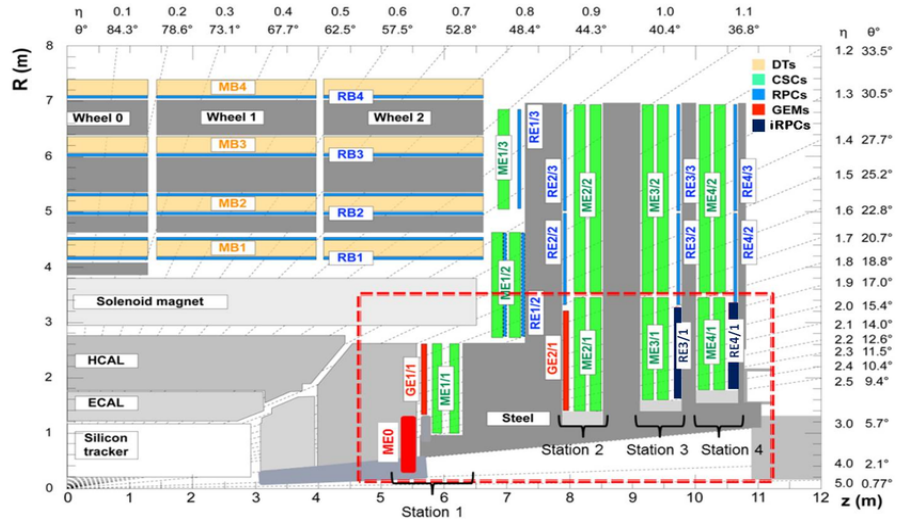


Figure 1.16: Location of the new GEM muon subsystem currently being installed in the very-forward region of CMS [86].

### 1.2.6 Trigger system

The CMS experiment is facing a data acquisition problem since the collision rate delivered by the LHC (one bunch crossing each 25ns, leading to an impressive rate of collisions of 40 MHz) is much larger than the data acquisition rate currently achievable by nowaday's electronics (around 1kHz only, more or less equivalent to 1Gb of data per second). It is therefore impossible to store and process all the collisions provided by the LHC ; instead, a selection needs to be made in order to

select and record only the most interesting events.

A system, called the trigger system, has therefore been put in place in order to select extremely quickly 1 kHz of interesting events out the 40MHz. This system is based on two different levels: first of all, the Level-1 Trigger (L1), a hardware set of electronics selecting around 100kHz of data, followed by the High-Level Trigger (HLT), a software layer improving the selection even more. Let's now give a bit more details about these two levels of trigger.

## Level-1 Trigger (L1)

The Level-1 Trigger (L1) is the first level of trigger, based directly on hardware. In order to maximize its efficiency, it is implemented in different subsystems of the detector (on the calorimeters and muons system) and in the service cavern, just next to the detector, so that the electric signals do not have to travel large distances, therefore saving a few precious nanoseconds of decision time.

This trigger, whose architecture is represented in Figure 1.17 gets new data each 25ns and today's electronics is not fast enough in order to deal with such a massive input of data, so an ingenious systems of buffers had to be put in place in order to put in line several events before analyzing all of them at once, using only basic segmented data provided by the detector.

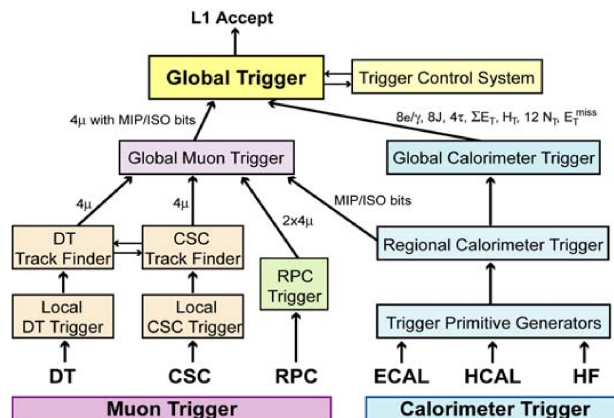


Figure 1.17: Architecture of Level-1 Trigger (L1) of CMS [86].

## High-Level Trigger (HLT)

On the other hand, the High-Level Trigger (HLT) does get access to the complete read-out data of the detector, since the rate has already been strongly reduced by the L1 Trigger, allowing it to perform complete calculations such as the ones that will be later performed offline. Since this is a software based layer and the decision time is not as critical any more, it runs on a farm of computers on the surface and is in constant evolution, getting constantly improvements and updates in order to select and reconstruct in a better and more efficient way interesting data from the collisions.

The HLT trigger is divided in several so-called **trigger paths**, especially developed in order to select a target object or physics process, usually with some  $p_T$  requirement in order to reduce

the statistics collected by any given trigger, to avoid passing the bandwidth limit of 1kHz. These triggers paths can then for example require the presence of one or two leptons, a jet whose  $p_T$  is higher to a certain threshold or the presence of Missing Transverse Energy (MET) in the event. If the selection implied by a trigger is too large, then it needs to be **prescaled**, meaning that its statistics is artificially reduced by forcing it to select one event every N, so that it does not use too much bandwidth: this is typically the case for trigger paths with low  $p_T$  requirements, as the ones used for the fake rate calculation explained in Section 2.4.3.

### 1.2.7 Data acquisition system

Finally, the CMS Data Acquisition System (DAQ), whose architecture is represented in Figure 1.18, has been designed to collect and analyze the data information at the nominal collision rate of 40MHz and is feeded directly from the Level-1 Trigger (L1). This means that it has to be able to read a flux of data of the order of 100kHz ( $\sim 100\text{Gb/s}$ ) coming from approximately 650 different sources at once, while providing enough computing power for the HLT to be able to reduce this rate by a factor  $\sim 100$ , while keeping resources for other tasks.

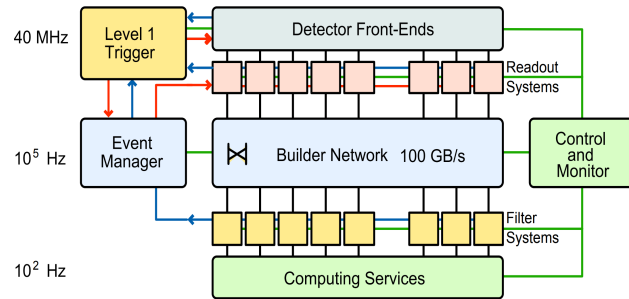


Figure 1.18: Architecture of CMS Data Acquisition System (DAQ) system [86].

The DAQ is also in charge of performing additional tasks, such as the generation of the Data Quality Monitoring (DQM) information resulting from online event processing in the HLT, the transfer of the data from local storage at the CMS site to mass storage in the CERN data centre at the Meyrin site and the operation of the Detector Control System (DCS) system, ensuring the correct operation of the detector and a high quality data taking at all times.



# Chapter 2

## Data, signals and backgrounds

In order to find a possible hint of the production of DM in the LHC collisions considering our signal models of interest, briefly described in Section ??, the data collected needs to be compared with Monte Carlo (MC) simulations produced in a central way for each SM process and mathematically able to simulate what is expected to be seen by the detector, taking into account the effect of the detector on the particles produced. This MC production method will be first of all briefly introduced in Section 2.1.

The different data samples collected during the Run II of operation of the LHC will be then detailed in Section 2.2, while the signal models and samples considered in this particular analysis and the MC samples used for the simulation of the different backgrounds will be introduced in Sections 2.3 and ?? respectively.

### 2.1 The Monte Carlo (MC) simulation method

The production and simulation of samples is a crucial step since most of the analyses performed at the LHC heavily depend on this MC generation to define the signal and background samples that can be directly compared with the data collected, in order to try and find eventual discrepancies which could be the hint of the presence of some BSM physics.

The basic idea of the MC simulation consists in using a random number generator in order to simulate as many events as computationally possible for all the SM processes, taking into account the probability density functions of the process being considered. This is performed by specific softwares called *event generators* and, of course, it is important to note that the perfect event generator does not exist, since we usually don't know everything about the SM or BSM process being generated.

The structure of a  $pp$  collision at the LHC as built up by event generators can actually be described by a few main steps that will now be described one by one, as shown in Figure 2.1. The interaction between the particles produced and the detector itself is then usually modeled using standard packages such as GEANT4 [101], able to completely describe this interaction or DELPHES 3 [102], able to provide a fast, yet approximate, simulation of a multipurpose detector.

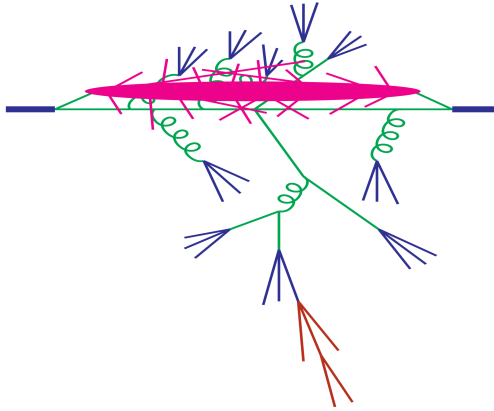


Figure 2.1: Structure of a  $pp$  collision and different steps of the MC simulation by the event generators, such as the parton shower (in green), the Underlying Event (UE) (in pink), the hadronization (in blue) and the decay of unstable particles (in red) [103].

### Hard scattering

Many processes of interest and expected to be produced by the LHC involve large momentum transfers, such as the production of jets with high transverse momenta or heavy particles. The simulation of such momenta transfers is therefore at the heart of the event generation and is usually referred to as the hard scattering process, the highest momentum transfer process in the event, whose probability distribution can be calculated using perturbation theory and several parameters, such as:

- The Parton Density Functions (PDFs)  $f_i(x, Q^2)$  of both partons involved in the collision, giving the probability of finding in the proton a parton of flavor  $i$  (quark or gluon) carrying a fraction  $x$  of the proton momentum with  $Q$  being the energy scale of the hard interaction [104]. Being universal, in the sense that the same PDFs enter in all the processes involving a given hadron, their main parameters are usually determined experimentally from hard-scattering data [105]. They are the key ingredient of the QCD parton model.
- The hard scattering matrix elements squared  $|\mathcal{M}_{pp \rightarrow n}|^2$ , usually evaluated considering all the Feynman diagrams of a given process, where  $n$  is the number of outgoing particles.

Many algorithms are then able to read such input parameters in order to compute the parton level cross section using different methods. The samples used in this work have actually been produced at different orders and by different hard scattering generators, such as MADGRAPH [106] (at Leading Order (LO)), POWHEG [107] and MC@NLO [108].

### Parton shower

The parton shower phase is used to describe what happens to the incoming and outgoing partons involved in the actual collision.

**Hadronization**

**Underlying Event (UE)**

**Unstable particle decays**

**GEANT**

**nanoAOD**

## **2.2 Data samples**

### **2.3 Signal samples**

### **2.4 Background prediction**

#### **2.4.1 The main background: $t\bar{t}$**

#### **2.4.2 Drell-Yan estimation**

#### **2.4.3 Non prompt contamination**

#### **2.4.4 Smaller backgrounds**

#### **2.4.5 Weights and corrections applied**



# Chapter 3

## Event selection

### 3.1 Signal regions

### 3.2 Control regions

### 3.3 Background-signal discrimination

#### 3.3.1 Discriminating variables

Missing Transverse Energy (MET)

MT2

#### 3.3.2 Neural network



# Chapter 4

## Results and interpretations

### 4.1 Systematics and uncertainties

### 4.2 Results



## Chapter 5

# Conclusions

### 5.1 Future prospects



# **Appendices**



# List of figures

1.1	LHC injection chain and experiments performed at CERN [83]. . . . .	3
1.2	Integrated luminosity collected by CMS over its different years of operation so far. . . . .	6
1.3	Mean PU distribution and luminosity recorded by CMS over the different years of operation of the LHC. . . . .	7
1.4	Schematic representation of the CMS detector, along with all its subdetectors and main characteristics. . . . .	8
1.5	Schematic representation of the CMS coordinate system used by convention. . . . .	9
1.6	Schematic representation of the CMS tracker, for different pseudorapidity values and along the z-axis [87]. . . . .	10
1.7	Tracker reconstruction efficiency of muons (on the left) and pions (on the right) for different pseudorapidities and particle momenta (1, 10 and 100 GeV) [86]. . . . .	11
1.8	Schematic representation of the sub-systems of the CMS ECAL [86]. . . . .	11
1.9	Schematic representation of a typical electromagnetic shower and the radiation length $X_0$ concept [86]. . . . .	12
1.10	Schematic representation of the HCAL sub-system in CMS [86]. . . . .	14
1.11	Distribution of the measured energy scaled to the incident energy for pions with incident energies of 200 GeV at $\eta = 0$ (on the left) and 225 GeV at $\eta = 0.5$ (on the right), with and without the inclusion of the HO in the HCAL system [86]. . . . .	14
1.12	Picture of the solenoid system of CMS being setup in the assembly hall. . . . .	15
1.13	Geometrical repartition along the z-axis of the different muons chambers in CMS [88].	16
1.14	Lateral geometrical division of the different DT chambers in one of the 5 wheels of CMS [86]. . . . .	17
1.15	Muon reconstruction efficiency with different $p_T$ and $\eta$ values, considering only the muon system (on the left), and the combined information from the muon system and the tracker (on the right) [86]. . . . .	19
1.16	Location of the new GEM muon subsystem currently being installed in the very-forward region of CMS [86]. . . . .	19

1.17	Architecture of Level-1 Trigger (L1) of CMS [86]. . . . .	20
1.18	Architecture of CMS Data Acquisition System (DAQ) system [86]. . . . .	21
2.1	Structure of a $pp$ collision and different steps of the MC simulation by the event generators, such as the parton shower (in green), the UE (in pink), the hadronization (in blue) and the decay of unstable particles (in red) [103]. . . . .	24

# List of tables

1.1	Expected and observed main parameters of $pp$ operation of the LHC across the different eras of operation [82]. . . . .	4
1.2	Comparison of the three main sub-systems currently used by CMS in order to identify muons [89]. . . . .	18



# Bibliography

- [1] F. Englert and R. Brout, "Broken symmetry and the mass of gauge vector mesons", Phys. Rev. Lett. 13, pp. 321-323, 1964
- [2] P. W. Higgs, "Broken symmetries and the masses of gauge bosons", Phys. Rev. Lett. 13, pp. 508-509, 1964
- [3] S. Chatrchyan et al., "Observation of a new boson at a mass of 125 GeV with the CMS experiment at the LHC", Phys. Lett. B716, pp. 30-61, 2012 [arXiv: 1207.7235]
- [4] G. Aad et al., "Observation of a new particle in the search for the Standard Model Higgs boson with the ATLAS detector at the LHC", Phys. Lett. B716, pp. 1-29, 2012 [arXiv: 1207.7214]
- [5] V.C. Rubin, W.K. Ford and N. Thonnard, "Rotational properties of 21 SC galaxies with a large range of luminosities and radii, from NGC 4605 (R=4kpc) to UGC 2885 (R=122kpc)", Astrophysical Journal 238, pp. 471-487, 1980
- [6] K.G. Begeman, A.H. Broeils and R.H. Sanders, "Extended rotation curves of spiral galaxies - Dark haloes and modified dynamics", Monthly Notices of the Royal Astronomical Society, vol. 249, issue 3, ISSN 0035-8711, 1991
- [7] A. Robertson, R. Massey and V. Eke, "What does the Bullet Cluster tell us about self-interacting dark matter?", Monthly Notices of the Royal Astronomical Society, vol. 465, issue 1, 2017 [arXiv: 1605.04307]
- [8] J.B. Mu?oz, C. Dvorkin and A. Loeb, "21-cm Fluctuations from Charged Dark Matter", Phys. Rev. Lett. 121, 121301 (2018) [arXiv: 1804.01092]
- [9] A. Natarajan, "A closer look at CMB constraints on WIMP dark matter", Phys. Rev. D85, 2012 [arXiv:1201.3939 ]
- [10] G. D'Ambrosio G.F. Giudice, G. Isidori and A. Strumia, "Minimal Flavour Violation: an effective field theory approach", Nucl.Phys. 645, pp 155-187, 2002 [arXiv:0207.036 ]
- [11] CMS Collaboration, "Search for the production of dark matter in association with top-quark pairs in the single-lepton final state in proton-proton collisions at  $\sqrt{s} = 8$  TeV", JHEP, vol. 6 121, 2015
- [12] CMS Collaboration, "Search for the Production of Dark Matter in Association with Top Quark Pairs in the Di-lepton Final State in pp collisions at  $\sqrt{s} = 8$  TeV", CMS-PAS-B2G-13-004, 2014

- [13] "Search for dark matter in events with heavy quarks and missing transverse momentum in pp collisions with the ATLAS detector", Eur. Phys. J. C (2015) 75:92
- [14] ATLAS Collaboration, Search for the Supersymmetric Partner of the Top Quark in the Jets+Emiss Final State at  $\sqrt{s} = 13$  TeV", ATLAS-CONF-2016-077
- [15] ATLAS Collaboration, "Search for top squarks in final states with one isolated lepton, jets, and missing transverse momentum in  $\sqrt{s} = 13$  TeV pp collisions with the ATLAS detector", ATLAS-CONF-2016-050, 2016
- [16] ATLAS Collaboration, "Search for direct top squark pair production and dark matter production in final states with two leptons in  $\sqrt{s} = 13$  TeV pp collisions using  $13.3 \text{ fb}^{-1}$  of ATLAS data", ATLAS-CONF-2016-076, 2016
- [17] ATLAS Collaboration, "Search for dark matter produced in association with bottom or top quarks in  $\sqrt{s} = 13$  TeV pp collisions with the ATLAS detector", Eur. Phys. J. C 78 (2018) 18 [arXiv: 1710.11412]
- [18] CMS Collaboration, Search for dark matter produced in association with heavy-flavor quark pairs in proton-proton collisions at  $\sqrt{s} = 13$  TeV", Eur. Phys. J. C (2017) 77: 845
- [19] CMS Collaboration, "Search for dark matter particles produced in association with a top quark pair at  $\sqrt{s} = 13$  TeV", Phys. Rev. Lett. 122, 011803 (2019) [arXiv: 1807.06522]
- [20] CMS Collaboration, "Search for dark matter produced in association with a single top quark or a top quark pair in proton-proton collisions at  $\sqrt{s} = 13$  TeV", JHEP, vol. 03 141, 2019 [arXiv: 1901.01553]
- [21] S. Manzoni, "The Standard Model and the Higgs Boson", Physics with Photons Using the ATLAS Run 2 Data, Springer Theses, 2019
- [22] A.B. Balantekin, A. Gouvea and B.Kayser, "Addressing the Majorana vs. Dirac Question with Neutrino Decays", FERMILAB-PUB-18-418-T, NUHEP-TH/18-09 [arXiv: 1808.10518]
- [23] J. Woithe, G.J. Wiener and F. Van der Vecken, "Let's have a coffee with the Standard Model of particle physics!", Physics education 52, number 3, 2017
- [24] F. Zwicky, "Die Rotverschiebung von extragalaktischen Nebeln", Helvetica Physica Acta , vol. 6, pp. 110-127, 1933
- [25] S. Van den Bergh, Phys Rev D "The early history of dark matter", Dominion Astrophysical Observatory, 1999
- [26] V.C. Rubin, W.K. Ford, "Rotation of the Andromeda Nebula from a Spectroscopic Survey of Emission Regions", Astrophysical Journal 159, p. 379, 1970
- [27] A. A. Penzias, R.W. Wilson, "A Measurement of Excess Antenna Temperature at 4080 Mc/s", Astrophysical Journal 142, pp. 419-421
- [28] D.J. Fixsen, "The temperature of the cosmic microwave background", Astrophysical Journal, 2009

- [29] Planck Collaboration, "Planck 2018 results. I. Overview and the cosmological legacy of Planck", 2018 [arXiv: 1807.06205]
- [30] R. Tojeiro, "Understanding the Cosmic Microwave Background Temperature Power Spectrum", 2006
- [31] Planck Collaboration, "Planck 2018 results. VI. Cosmological parameters", 2018 [arXiv: 1807.06209]
- [32] "Astrophysical Constants and Parameters", 2019
- [33] D. Clowe et all., "A Direct Empirical Proof of the Existence of Dark Matter", *Astrophysical Journal Letters* 648, 2006
- [34] K.R. Dienes, J. Fennick, J. Kumar, B. Thomas "Dynamical Dark Matter from Thermal Freeze-Out", *Phys. Rev. D* 97, 063522 (2018) [arXiv: 1712.09919]
- [35] C.S. Frenk, S.D.M. White, "Dark matter and cosmic structure", *Annalen der Physik*, p. 22 , 2012 [arXiv: 1210.0544]
- [36] R. Kirk, "Dark matter genesis"
- [37] M. Drewes et all., "A White Paper on keV Sterile Neutrino Dark Matter", 2016 [arXiv: 1602.04816]
- [38] C. Alcock et all., "The MACHO Project: Microlensing Results from 5.7 Years of LMC Observations", *Astrophys.J.* 542 (2000) 281-307
- [39] P. Tisserand et all., "Limits on the Macho content of the Galactic Halo from the EROS-2 Survey of the Magellanic Clouds", *A & A* 469, pp. 387-404 (2007)
- [40] EROS and MACHO collaborations, "EROS and MACHO Combined Limits on Planetary Mass Dark Matter in the Galactic Halo", 1998
- [41] Particle Data Group, "Neutrino Cross Section Measurements", PDG 2019
- [42] K. McFarland, "Neutrino Interactions", 2008 [arXiv: 0804.3899]
- [43] E. Morgante, "Aspects of WIMP Dark Matter Searches at Colliders and Other Probes", Springer theses, 2016
- [44] F. Couchot et all., "Cosmological constraints on the neutrino mass including systematic uncertainties", *A & A* 606, A104 (2017)
- [45] E. Bulbul et all., "Detection of An Unidentified Emission Line in the Stacked X-ray spectrum of Galaxy Clusters", 2014 [arXiv: 1402.2301]
- [46] A. Boyarsky et all., "An unidentified line in X-ray spectra of the Andromeda galaxy and Perseus galaxy cluster", *Phys. Rev. Lett.* 113, 251301 (2014) [arXiv: 1402.4119]
- [47] A. Boyarsky et all., "Checking the dark matter origin of 3.53 keV line with the Milky Way center", *Phys. Rev. Lett.* 115, 161301 (2015) [arXiv: 1408.2503]

- [48] T. Jeltema1 and S. Profumo, "Deep XMM Observations of Draco rule out at the 99% Confidence Level a Dark Matter Decay Origin for the 3.5 keV Line", 2015 [arXiv: 1512.01239]
- [49] D. Wu, "A Brief Introduction to the Strong CP Problem", Superconducting Super Collider Laboratory, 1991
- [50] R.D. Peccei, H.R. Quinn, "CP Conservation in the Presence of Pseudoparticles", Phys. Rev. Lett. 38, 1440, 1977
- [51] P.W. Graham et all., "Experimental Searches for the Axion and Axion-like Particles", Annual Review of Nuclear and Particle Science 65, 2015 [arXiv: 1602.00039]
- [52] CAST collaboration, "New CAST limit on the axion-photon interaction", Nature Physics 13, pp. 584-590 (2017)
- [53] B. Penning, "The Pursuit of Dark Matter at Colliders - An Overview", 2017 [arXiv: 1712.01391]
- [54] M. Schumann, "Direct Detection of WIMP Dark Matter: Concepts and Status", J. Phys. G46 (2019) no.10, 103003 [arXiv: 1903.03026]
- [55] S.C. Martin et all., "The RAVE survey: constraining the local Galactic escape speed", Mon.Not.Roy.Astron.Soc.379:755-772, 2007
- [56] K. Freese, M. Lisanti, C. Savage, "Annual Modulation of Dark Matter: A Review", [arXiv: 1209.3339v3]
- [57] T.M. Undagoitia and L. Rauch, "Dark matter direct-detection experiments", J. Phys. G43 (2016) no.1, 013001 [arXiv: 1509.08767]
- [58] R. Bernabei et all., "First results from DAMA/LIBRA and the combined results with DAMA/NaI", Eur.Phys.J.C56:333-355, 2008 [arXiv: 0804.2741]
- [59] J.M. Gaskins, "A review of indirect searches for particle dark matter", Contemporary Physics, 2016 [arXiv: 1604.00014]
- [60] F.S. Queiroz, "Dark Matter Overview: Collider, Direct and Indirect Detection Searches", Max-Planck Institute of Physics
- [61] LAT collaboration, "Constraints on Dark Matter Annihilation in Clusters of Galaxies with the Fermi Large Area Telescope", JCAP 05(2010)025 [arXiv: 1002.2239]
- [62] A.A. Moiseev et all., "Dark Matter Search Perspectives with GAMMA-400", 2013 [arXiv: 1307.2345]
- [63] L. Covi et all., "Neutrino Signals from Dark Matter Decay", JCAP 1004:017, 2010 [arXiv: 0912.3521]
- [64] B. Lu and H. Zong, "Limits on the Dark Matter from AMS-02 antiproton and positron fraction data", Phys. Rev. D 93, 103517 (2016) [arXiv: 1510.04032]

- [65] J. Abdallah et all., "Simplified Models for Dark Matter Searches at the LHC", Phys. Dark Univ. 9-10 (2015) 8-23 [arXiv: 1506.03116]
- [66] H. An, L. Wang, H. Zhang, "Dark matter with t-channel mediator: a simple step beyond contact interaction", Phys. Rev. D 89, 115014 (2014) [arXiv: 1308.0592]
- [67] ATLAS Collaboration, "Search for dark matter and other new phenomena in events with an energetic jet and large missing transverse momentum using the ATLAS detector", JHEP 01 (2018) 126 [arXiv: 1711.03301]
- [68] CMS Collaboration, "Search for new physics in the monophoton final state in proton-proton collisions at  $\sqrt{s} = 13$  TeV", J. High Energy Phys. 10 (2017) 073 [arXiv: 1706.03794]
- [69] CMS Collaboration, "Search for dark matter produced with an energetic jet or a hadronically decaying W or Z boson at  $\sqrt{s} = 13$  TeV", JHEP 07 (2017) 014 [arXiv: 1703.01651]
- [70] CMS Collaboration, "Search for new physics in final states with an energetic jet or a hadronically decaying W or Z boson and transverse momentum imbalance at  $\sqrt{s} = 13$  TeV", Phys. Rev. D 97, 092005 (2018) [arXiv: 1712.02345]
- [71] ATLAS Collaboration, "Search for dark matter in association with a Higgs boson decaying to two photons at  $\sqrt{s} = 13$  TeV with the ATLAS detector", Phys. Rev. D 96 (2017) 112004 [arXiv: 1706.03948]
- [72] CMS Collaboration, "Search for associated production of dark matter with a Higgs boson decaying to  $b\bar{b}$  or  $\gamma\gamma$  at  $\sqrt{s} = 13$  TeV", JHEP 10 (2017) 180 [arXiv: 1703.05236]
- [73] Atlas Collaboration, "Search for new phenomena in dijet events using 37 fb<sup>71</sup> of pp collision data collected at  $\sqrt{s} = 13$  TeV with the ATLAS detector", Phys. Rev. D 96, 052004 (2017) [arXiv: 1703.09127]
- [74] CMS Collaboration, "Search for narrow and broad dijet resonances in proton-proton collisions at  $\sqrt{s} = 13$  TeV and constraints on dark matter mediators and other new particles", JHEP 08 (2018) 130 [arXiv: 1806.00843]
- [75] C. Munoz, "Models of Supersymmetry for Dark Matter", FTUAM 17/2, IFT-UAM/CSIC-17-005, 2017 [arXiv: 1701.05259]
- [76] CMS Collaboration, "Searches for invisible decays of the Higgs boson in pp collisions at  $s_{\text{sqrt}s} = 7, 8,$  and  $13$  TeV", JHEP 02 (2017) 135 [arXiv: 1610.09218]
- [77] J. Alimena et all., "Searching for long-lived particles beyond the Standard Model at the Large Hadron Collider", 2019 [arXiv: 1903.04497]
- [78] A. Albert et all., "Recommendations of the LHC Dark Matter Working Group: Comparing LHC searches for heavy mediators of dark matter production in visible and invisible decay channels", 2017 [arXiv: 1703.05703]
- [79] M. Tanabashi et al., Particle Data Group, Phys. Rev. D98, 030001 (2018)
- [80] R. Schicker, "The ALICE detector at LHC", 2005

- [81] LHCb Collaboration, "LHCb Detector Performance", *Int. J. Mod. Phys. A* 30, 1530022 (2015) [arXiv: 1412.6352]
- [82] J.T. Boyd, "LHC Run-2 and Future Prospects", 2020
- [83] E. Gschwendtner, "AWAKE, A Particle-driven Plasma Wakefield Acceleration Experiment", CERN Yellow Report CERN 2016-001, pp.271-288 [arXiv: 1705.10573]
- [84] M. Thomson, "Modern Particle Physics", Cambridge University Press, 2013
- [85] G. Apollinari et all., "High Luminosity Large Hadron Collider HL-LHC", CERN Yellow Report CERN-2015-005, pp.1-19 [arXiv: 1705.08830]
- [86] CMS Collaboration, "The CMS experiment at the CERN LHC", *JINST* 3 (2008) S08004
- [87] CMS Collaboration, "Precision measurement of the structure of the CMS inner tracking system using nuclear interactions", *JINST* 13 (2018) P10034 [arXiv: 1807.03289]
- [88] M.S. Kim, "CMS reconstruction improvement for the muon tracking by the RPC chambers", 2013 *JINST* 8 T03001 [arXiv: 1209.2646]
- [89] CMS Collaboration, "Performance of the CMS muon detector and muon reconstruction with proton-proton collisions at  $\sqrt{s} = 13$  TeV", *JINST* 13 (2018) P06015 [arXiv: 1804.04528]
- [90] CMS Collaboration, "Particle-Flow Event Reconstruction in CMS and Performance for Jets, Taus, and MET", CMS-PAS-PFT-09-001, 2009
- [91] CMS Collaboration, "Description and performance of track and primary-vertex reconstruction with the CMS tracker", *JINST* 9 (2014) P10009 [arXiv: 1405.6569]
- [92] V. Knunz, "Measurement of Quarkonium Polarization to Probe QCD at the LHC", Springer theses, 2015
- [93] CMS Collaboration, "Performance of electron reconstruction and selection with the CMS detector in proton-proton collisions at  $\sqrt{s} = 8$  TeV", *JINST* 10 (2015) P06005 [arXiv: 1502.02701]
- [94] J. Rembser, "CMS Electron and Photon Performance at 13 TeV", *J. Phys. Conf. Ser.* 1162 012008, 2019
- [95] P.L.S. Connor, "Review of jet reconstruction algorithms", Ryan Atkin *J. Phys. Conf. Ser.* 645 012008, 2015
- [96] CMS Collaboration, "Jet energy scale and resolution in the CMS experiment in pp collisions at 8 TeV", *JINST* 12 (2017) P02014 [arXiv: 1607.03663]
- [97] F. Beaudette, "The CMS Particle Flow Algorithm", 2014 [arXiv: 1401.8155]
- [98] CMS Collaboration, "Identification of heavy-flavour jets with the CMS detector in pp collisions at 13 TeV", *JINST* 13 (2018) P05011 [arXiv: 1712.07158]
- [99] CMS Collaboration, "Performance of missing transverse momentum reconstruction in proton-proton collisions at  $\sqrt{s} = 13$  TeV using the CMS detector", *JINST* 14 (2019) P07004 [arXiv: 1903.06078]

- [100] L. Sonnenschein, "Analytical solution of ttbar dilepton equations", Phys.Rev.D73:054015, 2016
- [101] V. Lefebure and S. Banerjee, "CMS Simulation Software Using Geant4", CMS-NOTE-1999-072, 1999
- [102] DELPHES 3 Collaboration, "DELPHES 3, A modular framework for fast simulation of a generic collider experiment", JHEP 1402 (2014) 057 [arXiv:1307.6346]
- [103] M.H. Seymour and M. Marx, "Monte Carlo Event Generators", MCnet-13-05, 2013 [arXiv:1304.6677]
- [104] R. Placakyte, "Parton Distribution Functions", 2011 [arXiv:1111.5452]
- [105] L. Del Debbio, "Parton distributions in the LHC era", The European Physical Journal Conferences 175(394), 2018
- [106] J. Alwall et all., "MadGraph 5 : Going Beyond", 2011 [arXiv:1106.0522]
- [107] C. Oleari, "The POWHEG-BOX", Nucl.Phys.Proc.Suppl.205-206:36-41 [arXiv:1007.3893]
- [108] S. Frixione et all., "The MC@NLO 4.0 Event Generator", CERN-TH/2010-216 [arXiv: 1010.0819]